Charge regulation in nanopore ionic field-effect transistors

Zhijun Jiang and Derek Stein*
Department of Physics, Brown University, Providence, Rhode Island 02912, USA
(Received 5 October 2010; revised manuscript received 14 January 2011; published 18 March 2011)

We studied the ionic conductance through Al_2O_3 nanopore transistors to probe the surface charge density and its dependence on the applied gate field. The observed conductance modulations are entirely attributable to the electrostatic field effect, and their dependence on pH, ionic strength, and gate voltage is described by a quantitative model. Importantly, these experiments revealed how reactive surface groups dominate the response of nanofluidic field-effect devices via a chemical effect called charge regulation. A quantitative understanding of this effect enables the development of new nanofluidic technologies.

DOI: 10.1103/PhysRevE.83.031203 PACS number(s): 66.10.Ed, 82.45.−h, 47.61.−k, 85.35.−p

I. INTRODUCTION

Solid-state nanopores have emerged as powerful tools for studying ion transport and single DNA molecules [1]. Electrical functionalization can add a new dimension to these studies. A gate electrode embedded in the supporting membrane of a nanopore can be used to electrostatically control the transport of charges through it, whether that transport be the flow of small ions or the translocation of polyions like DNA. It has even been theorized that DNA translocations can be manipulated at the level of single bases using electrostatic forces [2]. The key to such applications lies in manipulating the charge at the solid-liquid interface.

The surface charge density σ in fact plays a crucial role in a wide range of micro- and nanofluidic systems, and it can be controlled using applied electric fields. Field-induced charging underlies electrokinetic phenomena such as induced-charge electro-osmosis (ICEO) and induced-charge electrophoresis [3], and it has been employed to control, for example, forces on charged colloids in solution [4], electro-osmotic flow in microchannels [5], the transport of charged proteins in nanoscale channels [6], and the conductance of narrow pores [7–11]. However, incorporating "electrofluidic" effects into sophisticated nanofluidic technologies requires a quantitative understanding of the field dependence of σ, which is lacking.

In this article, we present a detailed experimental and theoretical characterization of ionic conductance gating in nanopore transistors. Ion transport through a nanopore is sensitive to σ because the screening layer of counterions that it attracts contributes significantly to the conductance and even dominates over the bulk conductance at low ionic strength [12]. We demonstrate nanopore ionic transistors whose conductance modulations arise purely from electrostatic field effects. Furthermore, the dependence of our measurements on pH and ionic strength highlights a crucial difference between ionic transistors and their semiconductor cousins: the reactive groups at the solid-liquid interface in a nanopore lead to a significant chemical response known as charge regulation. Agreement between the experimental results and a theoretical model we recently developed to account for charge regulation shows that a quantitative understanding of electrofluidic gating has been achieved [13].

*Derek_Stein@Brown.edu

II. NANOPORE TRANSISTOR FABRICATION AND CHARACTERIZATION METHODS

Solid-state nanopores with embedded gate electrodes (sketched in cross section in Fig. 1) were fabricated following a procedure described elsewhere in detail [14]. Briefly, a 20-nm-thick, free-standing membrane of silicon nitride was formed on top of an 800-nm-thick supporting stack of silicon dioxide and silicon nitride, which was in turn supported on a silicon substrate. A patterned, 30-nm-thick, planar Cr gate electrode was deposited on the membrane using standard photolithography and metal evaporation. A ∼70-nm-diameter pore was subsequently milled through the electrode and membrane using a focused ion beam (FIB) machine. The device was then coated with 25 nm of aluminum oxide (Al_2O_3) by atomic layer deposition (ALD), which insulated the Cr electrode. The epitaxial ALD deposition process reduced the final diameter of the pore to ∼20 nm, as measured by transmission electron microscopy (TEM).

An ionic transistor (Fig. 1) was created by contacting the gated nanopore chip on either side to reservoirs of ionic solution. Ag/AgCl electrodes were inserted into the top (source) and bottom (drain) reservoirs. The electrochemical potential between the source and drain, V_{sd}, was controlled using a current amplifier (Axon Axopatch 200B) that also monitored the ionic current through the pore, I_{sd}. A second current amplifier (SRS 570), connected to the embedded gate electrode, charged the gate to a potential V_g while monitoring the current I_g flowing into it. Devices were characterized by measuring I_{sd} and I_g as functions of V_{sd} and V_g. Sweeps of V_{sd} from 0 to 0.2 V were performed in steps of 0.04 V lasting 10 s each. V_g was increased from −0.5 to 0.5 V in 0.1-V intervals between V_{sd} sweeps. The limited ranges of V_g and V_{sd} tested did not cause dielectric breakdown of the gate insulator [13]. We focused on the steady-state behavior of devices by determining I_{sd} and I_g from the average of the last 2 s of data, which excluded current transients that followed changes in the applied potentials.

Wide ranges of pH and ionic strength n were tested: 1-mM potassium chloride (KCl) solutions were buffered to pH = 3, 5, 8, and 10 using 1 mM of glycine-HCl ($pK = 2.34$), acetic acid-sodium acetate ($pK = 4.76$), Tris-HCl ($pK = 8.1$), and glycine-KOH ($pK = 9.6$), respectively. A 10-mM glycine-HCl buffer maintained $pH = 3$ in the presence of 10-mM, 100-mM, and 1-M KCl, for which n was calculated to be

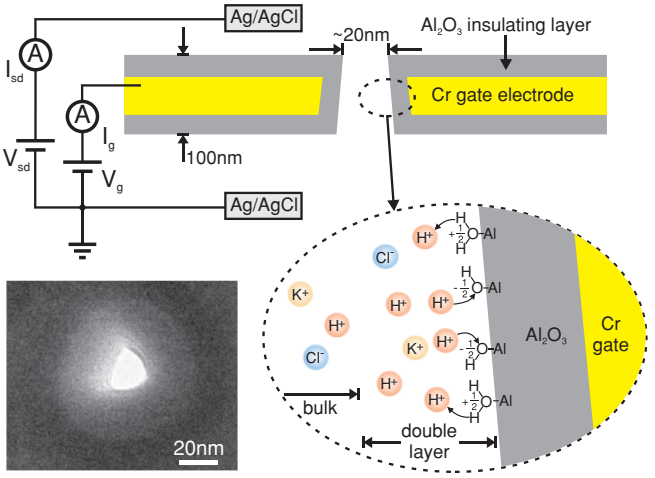

FIG. 1. (Color online) Nanopore ionic transistor. Ionic current was driven through a nanopore by an applied source-drain potential V_{sd} and was modulated by a gate potential V_g applied to an embedded electrode surrounding the nanopore. The source-drain current I_{sd} and the gate current I_g were measured simultaneously. A zoom-in of the nanopore sketches the effective chemistry of the Al_2O_3 surface. Inset: TEM image of the nanopore used to obtain the data presented in Figs. 2, 3, and 5.

13 mM, 103 mM, and 1.003 M, respectively, given the pK of glycine. The ionic strength for 1-mM KCl buffered at pH = 3 was 2.2 mM. The devices were cleaned, both initially and between tests of different solutions, by flushing both reservoirs with degassed, deionized water, then isopropanol, and then again with deionized water. More aggressive cleaning agents like oxygen plasma and piranha solution were avoided because they apparently degraded the gate dielectric, often leading to large leakage conductances.

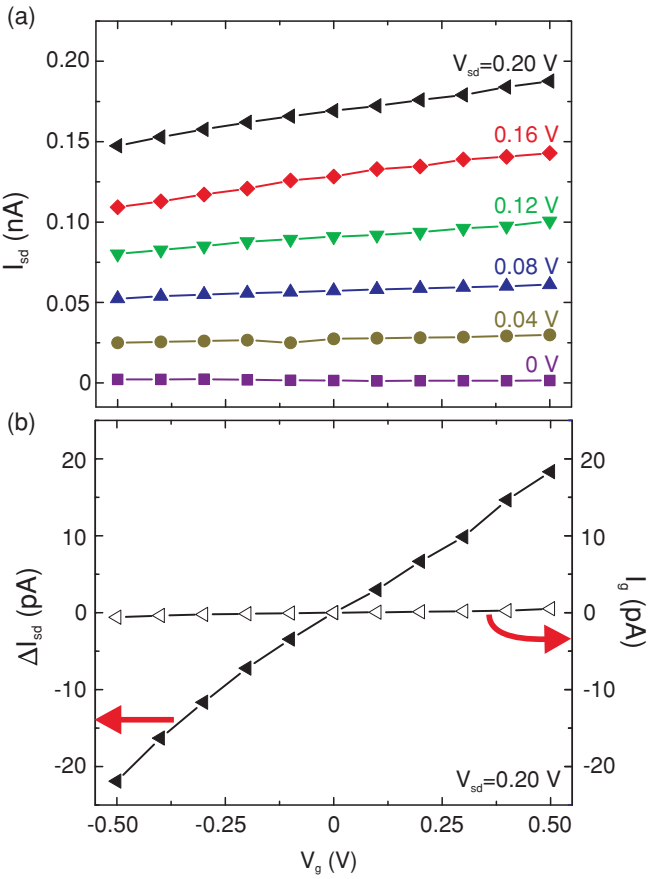

FIG. 2. (Color online) Electrofluidic gating in a 16-nm-wide nanopore transistor. (a) The V_g-dependence of I_{sd} at 1-mM KCl and pH = 3 is plotted for the various V_{sd} indicated. (b) I_g and ΔI_{sd}, which is the change in I_{sd} relative to its value at $V_g = 0$ V, are plotted against V_g for $V_{sd} = 0.2$ V.

III. EXPERIMENTAL OBSERVATIONS AND THEORETICAL MODELING

Clear evidence of field-effect control over the conductance of a 16-nm-wide nanopore device (Fig. 1, TEM image) can be seen in Fig. 2, which shows the gating characteristics in a 1-mM KCl solution at pH = 3. I_{sd} increased with V_g for all V_{sd}, exhibiting a $\approx 24\%$ conductance change over the 1-V range of V_g [Fig. 2(a)]. Over that range, the applied gate field E_g increased by $\approx 4 \times 10^{-7}$ V/m. The variation in I_{sd} with V_g was not caused by leakage to the gate electrode, which was negligible in our experiments ($I_g < 2$ pA for all experiments reported here). Figure 2(b) compares I_g to the gate-induced change in I_{sd} (relative to $V_g = 0$ V), measured simultaneously at $V_{sd} = 0.2$ V. The large swing in I_{sd} was entirely attributable to the electrofluidic field effect.

The pH dependence of the nanopore transistor reveals the important role played by surface chemistry in electrofluidic gating. Figure 3 plots I_{sd} against V_g for different pH values of a 1-mM KCl buffer at $V_{sd} = 0.2$ V. The slope of the curve, representing the response of σ to E_g, decreased with pH and even flipped sign. The measured slope was large and positive at pH = 3, lower for pH = 5, small and negative for pH = 8, and large and negative for pH = 10. Furthermore, the conductance of the unbiased device varied nonmonotonically with pH. The conductance reached a minimum at an intermediate pH = 8.

Similar I_{sd} gating was observed in 11 of the 21 devices tested. No gating response was observed in 10 devices, possibly due to interruption of the electrical connection to the perimeter of the gate electrode.

The behavior observed in Figs. 2 and 3 has a straightforward interpretation: The surface conductance of the nanopore is governed by σ, to which capacitive charging by the gate and chemical surface charges both contribute. The surface chemistry of Al_2O_3 imparts an intrinsic positive σ at pH = 3 and 5, which increases with V_g. At pH = 8 and 10, on the other hand, the surface is intrinsically negatively charged; therefore, increasing V_g acts to neutralize the surface. The relationship between σ, V_g, and the properties of the buffer is therefore determined by the interplay between capacitive charging, the chemical charge density, and, importantly, charge regulation, which is the field-induced shift in the chemical equilibrium that we recently included in a quantitative model [13].

Our model considers a metal electrode separated from the solution by an oxide insulator, where the "standard model" of the double layer is applied [Fig. 4(a)] The innermost layer of counterions is known as the Stern layer, which is

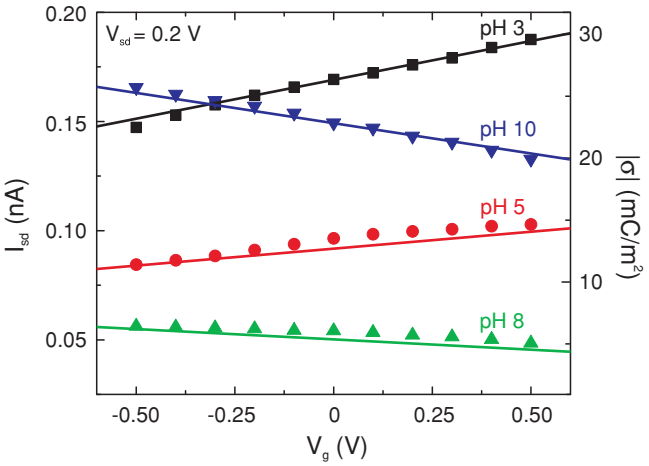

FIG. 3. (Color online) Dependence of electrofluidic gating on pH. I_{sd} is plotted against V_g for 1-mM KCl buffers at pH = 3, 5, 8, and 10, and for $V_{sd} = 0.2$ V. The 1-pK electrofluidic gating model for σ, combined with PNP simulations of the ion transport, were fit to the data (solid lines). The right axis shows $|\sigma|$.

tightly bound to the surface. The Stern layer is separated from the surface by an effective distance comparable to the ionic radius. The electrochemical potential at the Stern layer is denoted ψ_{DL}. The diffuse layer is the portion of the electric double layer that extends farther away from the surface, where the electrochemical potential decays to the bulk value V_b. A potential applied between the gate (V_g) and the bulk electrolyte (V_b) falls across three elements in series [Fig. 4(b)]: (1) a capacitor C_I representing the oxide insulator separating the gate from the electrolyte, (2) the phenomenological Stern-layer capacitance C_S accounting for the dielectric properties of the insulator-liquid interface, and (3) the electrolyte, described by the nonlinear Poisson-Boltzmann (PB) theory. The chemistry of the Al_2O_3 surface is described by a 1-pK model in which the protonation and deprotonation of hydroxyl groups proceeds according to the single-step dissociation reaction (illustrated in Fig. 1) [15–18]:

$$\mathrm{Al\cdot OH}^{-1/2} + \mathrm{H}^+ \rightleftharpoons \mathrm{Al\cdot OH}_2^{+1/2}. \tag{1}$$

Chemical equilibrium between the surface and the adjacent electrolyte is given by

$$\frac{[\mathrm{H}^+]_0 \Gamma^{\mathrm{AlOH}^{-1/2}}}{\Gamma^{\mathrm{AlOH}_2^{+1/2}}} = 10^{-\mathrm{p}K}, \tag{2}$$

where $\Gamma^{\mathrm{AlOH}^{-1/2}}$ and $\Gamma^{\mathrm{AlOH}_2^{+1/2}}$ are the densities of surface groups in their negatively and positively charged states, respectively, and pK is the dissociation constant. The proton activity at the surface, $[\mathrm{H}^+]_0$, is related to the potential there, ψ_0, and the pH of the solution by a Boltzmann factor, $[\mathrm{H}^+]_0 = 10^{-\mathrm{pH}} \exp(-\frac{e\psi_0}{k_B T})$, where e is the charge quantum and $k_B T$ is the thermal energy. The sum of the chemical surface charge density $\sigma_C = \frac{1}{2}e(\Gamma^{\mathrm{AlOH}_2^{+1/2}} - \Gamma^{\mathrm{AlO}^{-1/2}})$, and the capacitive charge at the surface gives σ.

The distributions of charge and potential have been solved. The procedure outlined in [13] accommodates the dissociation reaction given by Eq. (1) with minor adjustments. We

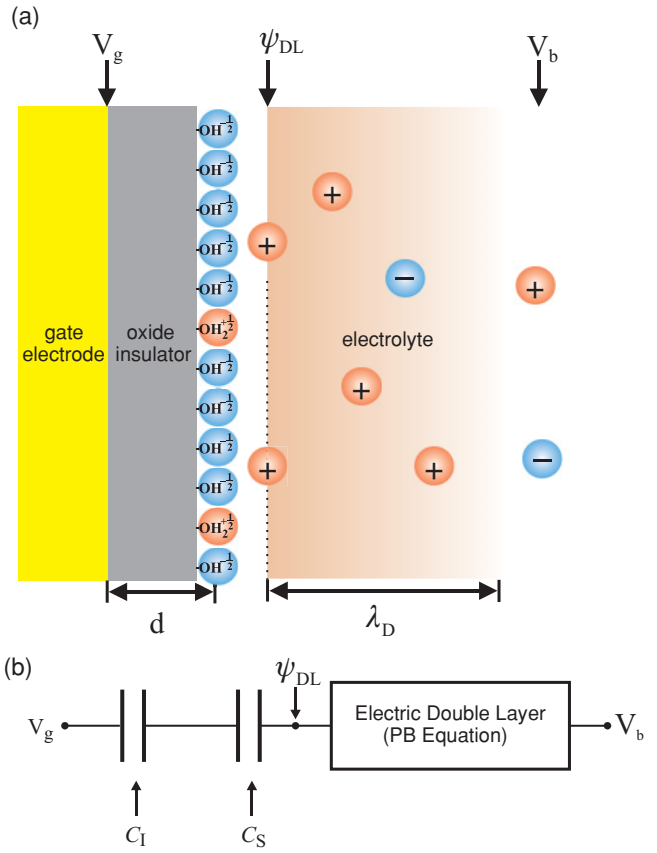

FIG. 4. (Color online) Modeling the inner surface of the nanopore. (a) Schematic shows the gate electrode separated from the electrolyte by an oxide insulator, whose surface contains chemically reactive hydroxyl groups. (b) In an equivalent circuit model, the oxide insulator and the Stern layer are capacitors C_I and C_S, respectively, and the electric double layer is a nonlinear element described by the Poisson-Boltzmann equation. The electrochemical potential is defined at the gate (V_g), at the double-layer (ψ_{DL}), and in the bulk electrolyte (V_b).

determine σ by first using the following equations relating σ_C to the potential on the liquid side of the solid-liquid interface, ψ_{DL}:

$$\sigma_C = \frac{e\Gamma_0}{2} \frac{\exp\left(\frac{e}{k_B T}\left[V_b - \frac{\sigma_C + C_I V_g + C_S \psi_{DL}}{C_I + C_S}\right]\right) - 10^{(\mathrm{pH}-\mathrm{p}K)}}{\exp\left(\frac{e}{k_B T}\left[V_b - \frac{\sigma_C + C_I V_g + C_S \psi_{DL}}{C_I + C_S}\right]\right) + 10^{(\mathrm{pH}-\mathrm{p}K)}}, \tag{3}$$

$$\sigma_C = \frac{C_I}{C} \frac{2k_B T \epsilon \epsilon_0}{\lambda_D e} \sinh\left(\frac{e(\psi_{DL} - V_b)}{2k_B T}\right) + C_I(\psi_{DL} - V_g). \tag{4}$$

Here, ϵ_0 is the permittivity of free space, ϵ is the dielectric constant of the electrolyte, $\lambda_D = \sqrt{\frac{\epsilon\epsilon_0 k_B T}{e^2 n}}$ is the Debye length, $\Gamma_0 \equiv \Gamma^{\mathrm{AlOH}_2^{+1/2}} + \Gamma^{\mathrm{AlOH}^{-1/2}}$ is the density of surface groups, and $C \equiv (C_I^{-1} + C_S^{-1})^{-1}$. We find ψ_{DL} from the intersection of the two σ_C vs. ψ_{DL} curves obtained by numerically evaluating

Eqs. (3) and (4). ψ_{DL} is in turn related to σ by the Grahame equation

$$\sigma = \frac{2k_BT\epsilon\epsilon_0}{\lambda_D e}\sinh\left(\frac{e(\psi_{\mathrm{DL}} - V_b)}{2k_BT}\right). \quad (5)$$

Ion transport through a nanopore of a known geometry and a uniform σ has been simulated using finite-element methods [19,20]. We followed this procedure, fixing σ with the electrofluidic gating model and defining the nanopore geometry as a truncated cone with a 5° vertex angle, measured by TEM tilting experiments (data not shown). Our finite-element simulations used COMSOL to solve the Poisson-Nernst-Planck (PNP) equations:

$$\nabla^2\psi = -\frac{1}{\epsilon\epsilon_0}\sum_i ez_ic_i, \quad (6)$$

$$\vec{J}_i = -D_i\left(\vec{\nabla}c_i + \frac{ez_ic_i}{k_BT}\vec{\nabla}\psi\right). \quad (7)$$

Here, $\vec{J}_i$, D_i, c_i, and z_i are the flux, diffusion constant, concentration, and valence of ion species i, respectively, and ψ is the electrochemical potential. The KCl buffer was approximated as pure KCl solution of equivalent n. The details of the simulation are described in the appendix. The PNP simulation used $\epsilon = 80$ for water, $T = 298$ K, and $D_{K^+} = D_{Cl^+} = 2 \times 10^{-9}$ m^2/s. The electrofluidic gating model used $V_b = \frac{1}{2}V_{sd}$, $C_S = 2.9$ F/m^2, and $C_I = 0.007$ F/m^2, obtained from $C_I = \frac{\epsilon_0\epsilon'}{a\ln(b/a)}$ for a cylindrical Al_2O_3 capacitor of inner diameter a, outer diameter b, and $\epsilon' = 9$. Γ_0 and the pK were fitting parameters. We note that this ion transport model ignores electro-osmotic flow and gradients in σ that would be induced by V_{sd}. These second-order effects presumably had a limited impact ($\leqslant 10\%$) on the conductance of the nanopore [20], perhaps shifting the fit values of Γ_0 and pK slightly.

The electrofluidic gating model and PNP ion transport simulations agree quantitatively with the measured behavior of the nanopore transistor over the full ranges of V_g and pH (Fig. 3). The two fitting parameters $\Gamma_0 = 3.5 \times 10^{17}$ m^{-2} and p$K = 6.93$ accurately captured the magnitude and sign of the changes in I_{sd} induced by V_g gating and yield values of σ (Fig. 3, right axis) that are consistent with the known properties of Al_2O_3 [21]. The pK and Γ_0 values obtained from the 10 other responsive nanopores were similar, ranging from 6.2 to 7.3 and 3.0 to 4.5×10^{17} m^{-2}, respectively, although the conductance at a single extreme pH occasionally departed from the predictions by up to ~30%.

To further test the model, we compared its predictions to the behavior of the nanopore transistor at different salt concentrations. Figure 5 plots the fractional change in I_{sd} with V_g (relative to $V_g = 0$ V) for 1-mM, 10-mM, 100-mM and 1-M KCl solutions at p$H = 3$ and for $V_{sd} = 0.2$ V. Field-effect control over the source-drain conductance was most effective at low n, with a $\approx 24\%$ change per volt achieved at 1-mM KCl, compared with less than 1% at 1-M KCl. The slopes of the experimental curves were well described by the model over the full range of n, using the same pK and Γ_0 values determined previously. The inset to Fig. 5 shows the n dependence of the conductance of the nanopore at $V_g = 0$ V, which was also well described by the model.

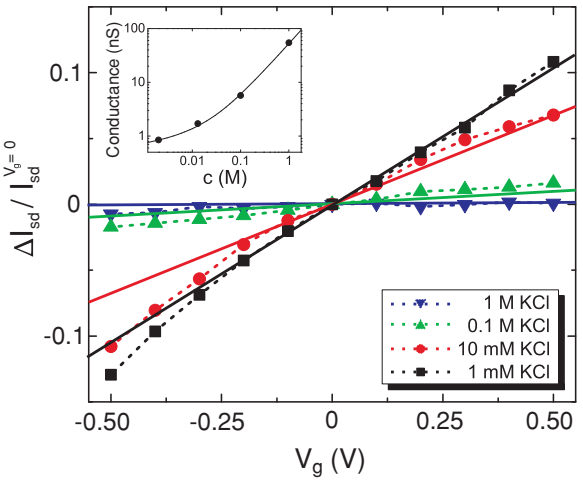

FIG. 5. (Color online) Salt dependence of electrofluidic gating. The fractional change in I_{sd} induced by V_g (relative to $V_g = 0$ V) is plotted for various KCl concentrations and $V_{sd} = 0.2$ V. The inset plots the n dependence of the source-drain conductance. The solid curves are predictions of the 1-pK electrofluidic gating model, using the same parameters as in Fig. 3.

IV. DISCUSSION

An important feature of this study is that the response of the nanopore transistors can be unambiguously attributed to the field effect, thanks to the simultaneous measurement of I_{sd} and negligible I_g. In previous studies of conductance gating, the confounding and possibly dominant effects of leakage currents either went unquantified [7–9] or clearly influenced the gating response [10,11]. Reported gating sensitivities, estimated from the relative change in the channel conductance for a given E_g, range from $\approx$0.6 V^{-1} nm [9] to $\approx$ 130 V^{-1} nm [11], and none were described by a quantitative model. By contrast, the typical sensitivity of our nanopore transistor was $\approx$5 V^{-1} nm, and the sign, magnitude, and dependence of the gating response on pH and salt concentration were all described by the electrofluidic gating model [13].

The central role played by surface chemistry was captured by a 1-pK model of Al_2O_3 that involves only two parameters. A 1-pK model should apply to most oxides, because it represents the lowest order in an expansion of the behavior of strongly interacting surface groups [17]. The pK we obtained is at the low end of the reported range for Al_2O_3: 6.9–10.0 [22], and Γ_0 is ~8 times lower than a previously reported value [23]. However, these parameters depend strongly on the preparation of the surface, and it is known that high temperatures, such as those used for ALD growth, can reduce the density of hydroxyl groups, leading to a relatively acidic surface with a low pK [24]. This fact can explain our findings.

It was pointed out by van Hal *et al.* that a chemically reactive surface acts as a buffer. Field-induced changes in σ are consequently smaller than would be expected from a naïve, inert capacitor model. This effect was illustrated in a recent study of ICEO over oxide surfaces, where the "buffer capacitance" was invoked to quantitatively explain

TABLE I. Boundary conditions and maximum mesh sizes for the numerical PNP ion transport simulation in the computational domain sketched in Fig. 6.

Surface	Nernst-Planck Eq.	Poisson Eq.	Maximum Mesh Size
1	axial symmetry	axial symmetry	0.5 nm
2, 10	axial symmetry	axial symmetry	100 nm
3	concentration $c_i = c_0$[a]	constant potential $V_0 = 0.2$ V	100 nm
4, 8	insulation $\mathbf{n} \cdot \mathbf{J} = 0$[b]	zero charge $\mathbf{n} \cdot \nabla V = 0$	100 nm
5, 7	insulation $\mathbf{n} \cdot \mathbf{J} = 0$	surface charge $\mathbf{n} \cdot \nabla V = \sigma$	10 nm
6	insulation $\mathbf{n} \cdot \mathbf{J} = 0$	surface charge $\mathbf{n} \cdot \nabla V = \sigma$	0.5 nm
9	concentration $c_i = c_0$	ground, $V_0 = 0$	100 nm

[a] i can be ionic species K^+ or Cl^-.
[b] $\mathbf{n}$ is the surface normal vector.

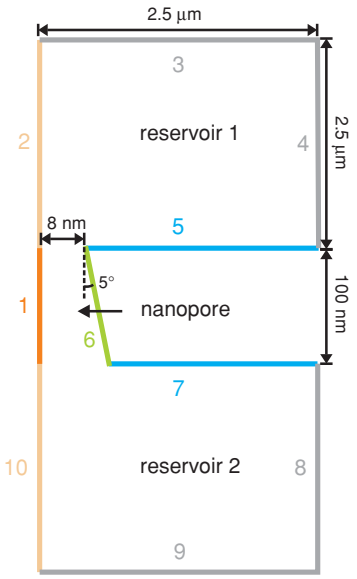

FIG. 6. (Color online) Cross section of one half of the cylindrically symmetric nanopore used for COMSOL simulation. The sketch illustrates the wall of the nanopore (green, surface 6), the axis of ration used to obtain the three-dimensional nanopore geometry (light and dark orange, surfaces 1, 2, and 10), the dielectric coating of the nanopore (blue, surfaces 5 and 7) and the boundaries of the two reservoirs (gray, surfaces 3, 4, 8, and 9). The boundary conditions and maximum mesh sizes of each surface are summarized in Table I.

the results [25]. In nanopore transistors, charge regulation at the surface explains why I_{sd} responded weakly to V_g, especially as the pH approached the pK (Fig. 3). The ICEO study, which probed the ac modulations of σ, and the present study of nanopore transistors, which probed $|\sigma|$, both showed quantitative agreement with similar chemical models of the surface [25]. These findings point to a converging picture of electrofluidic effects.

V. CONCLUSION

In conclusion, we have demonstrated a nanopore ionic transistor whose conductance was exclusively controlled by an electrostatic field effect and whose behavior was quantitatively described by an electrofluidic gating model that includes the dominant effects of charge regulation. These results have clear technological implications. The field effect can be employed in nanofluidic devices based on the materials and fabrication methods of standard integrated circuits. There is now a quantitative understanding of the relationship between the applied gate field and σ at oxide surfaces, which lies at the heart of such applications.

ACKNOWLEDGMENTS

This work was supported by NSF grant DMR-0805176. Z. J. acknowledges support from the NSF RI-EPSCoR program.

APPENDIX

Simulation of the ion transport through a nanopore of a known geometry and a uniform surface charge density were performed with COMSOL Multiphysics Software (Version 3.2a). The Electrostatic Module, which implements the Poisson equation, and the Nernst-Planck without the Electroneutrality Module were used. A two-dimensional cylindrically symmetric nanopore geometry was modeled for computational efficiency. Figure 6 shows the geometry of the 100-nm-long nanopore (green), sandwiched between two fluidic reservoirs. The boundary conditions for the Nernst Planck equation and the Poisson equation, as well as the maximum mesh size for each surface are summarized in Table I. The DIRECT (UMFPACK) time-independent solver was used. The total number of meshes was ~15 k. The number of degrees of freedom was ~100 k.

[1] C. Dekker, Nature Nanotechnology **2**, 209 (2007).
[2] S. Polonsky, S. Rossnagel, and G. Stolovitzky, Appl. Phys. Lett. **91**, 153103 (2007).
[3] M. Z. Bazant and T. M. Squires, Curr. Opin. Colloid Interface Sci. **15**, 203 (2010).
[4] A. C. Hillier, S. Kim, and A. J. Bard, J. Phys. Chem. **100**, 18808 (1996).
[5] R. Schasfoort, S. Schlautmann, J. Hendrikse, and A. van den Berg, Science **286**, 942 (1999).
[6] R. Karnik, K. Castelino, and A. Majumdar, Appl. Phys. Lett. **88**, 123114 (2006).

[7] R. B. Schoch and P. Renaud, Appl. Phys. Lett. **86**, 253111 (2005).
[8] R. Karnik, R. Fan, M. Yue, D. Li, P. Yang, and A. Majumdar, Nano Lett. **5**, 943 (2005).
[9] R. Fan, M. Yue, R. Karnik, A. Majumdar, and P. Yang, Phys. Rev. Lett. **95**, 086607 (2005).
[10] R. Fan, S. Huh, R. Yan, J. Arnold, and P. Yang, Nature Mater. **7**, 303 (2008).
[11] S. W. Nam, M. J. Rooks, K. B. Kim, and S. M. Rossnagel, Nano Lett. **9**, 2044 (2009).
[12] D. Stein, M. Kruithof, and C. Dekker, Phys. Rev. Lett. **93**, 035901 (2004).
[13] Z. Jiang and D. Stein, Langmuir **26**, 8161 (2010).
[14] Z. Jiang, M. Mihovilovic, J. Chan, and D. Stein, J. Phys. Condens. Matter **22**, 454114 (2010).
[15] T. Hiemstra, W. H. V. Riemskijk, and G. H. Bolt, J. Colloid Interface Sci. **133**, 91 (1989).
[16] R. E. G. van Hal, J. C. T. Eijkel, and P. Bergveld, Adv. Colloid Interface Sci. **69**, 31 (1996).
[17] M. Borkovec, Langmuir **13**, 2608 (1997).
[18] P. M. Biesheuvel, M. van der Veen, and W. Norde, J. Phys. Chem. B **109**, 4172 (2005).
[19] D. Constantin and Z. S. Siwy, Phys. Rev. E **76**, 041202 (2007).
[20] H. S. White and A. Bund, Langmuir **24**, 2212 (2008).
[21] R. Sprycha, J. Colloid Interface Sci. **127**, 1 (1989).
[22] M. Kosmulski, *Encyclopedia of Surface and Colloid Science* 2nd ed., edited by P. Somasundaran (CRC Press, 2006).
[23] J. G. Larson and W. K. Hall, J. Phys. Chem. **69**, 3080 (1965).
[24] G. Sposito, *The Environmental Chemistry of Aluminium*, 2nd ed. (CRC Press, 1995).
[25] A. J. Pascall and T. M. Squires, Phys. Rev. Lett. **104**, 088301 (2010).